Journal of Power Sources 196 (2011) 287–300

Contents lists available at ScienceDirect

Journal of Power Sources

journal homepage: www.elsevier.com/locate/jpowsour

Pore-scale modeling of the reactive transport of chromium in the cathode of a solid oxide fuel cell

E.M. Ryan [a,b,*], A.M. Tartakovsky [b], K.P. Recknagle [b], M.A. Khaleel [b], C. Amon [a,c]

[a] Carnegie Mellon University, Department of Mechanical Engineering, Scaife Hall, 5000 Forbes Avenue, Pittsburgh, PA 15213, USA
[b] Pacific Northwest National Laboratory, Computational Science and Mathematics Division, P.O. Box 999, Richland, WA 99352, USA
[c] Faculty of Applied Science & Engineering, University of Toronto, Galbraith Building, Room 170, 35 St. George Street, Toronto, Ontario, Canada M5S 1A4

ARTICLE INFO

Article history:
Received 10 March 2010
Received in revised form 10 June 2010
Accepted 11 June 2010
Available online 22 June 2010

Keywords:
Solid oxide fuel cell
Computational modeling
Chromium poisoning
Reactive transport
Competitive adsorption

ABSTRACT

We present a pore-scale model of a solid oxide fuel cell (SOFC) cathode. Volatile chromium species are known to migrate from the current collector of the SOFC into the cathode where over time they decrease the voltage output of the fuel cell. A pore-scale model is used to investigate the reactive transport of chromium species in the cathode and to study the driving forces of chromium poisoning. A multi-scale modeling approach is proposed which uses a cell level model of the cathode, air channel and current collector to determine the boundary conditions for a pore-scale model of a section of the cathode. The pore-scale model uses a discrete representation of the cathode to explicitly model the surface reactions of oxygen and chromium with the cathode material. The pore-scale model is used to study the reaction mechanisms of chromium by considering the effects of reaction rates, diffusion coefficients, chromium vaporization, and oxygen consumption on chromium's deposition in the cathode. The study shows that chromium poisoning is most significantly affected by the chromium reaction rates in the cathode and that the reaction rates are a function of the local current density in the cathode.

1. Introduction

Solid oxide fuel cells (SOFCs) are currently being developed as an alternative to traditional fossil fuel burning power plants and show promise as a cleaner, more efficient alternative energy technology. SOFCs have been shown to have an electrical efficiency of 35–43% and are expected to reach 50–60% electrical efficiency [1].

In recent years the operating temperatures of SOFCs have been reduced to 600–1000 °C which allows for stainless steel current collectors to be used. Stainless steel is a less expensive alternative to the ceramic current collectors used in earlier SOFC designs, and is easy to machine, has a high electrical conductivity, and is able to withstand the corrosive environment of the fuel cell. The stainless steels typically used in SOFCs contain chromium which forms a protective chromia oxide scale on the current collector. These stainless steels are chosen because of the low electrical resistance of the chromia oxide scale, which does not significantly increase the ohmic losses in the fuel cell. However, the chromia oxide scale has been shown to react with the air in the air channel of the cathode to form volatile chromium species [2]. Chromium poisoning occurs when these volatile chromium species, typically $CrO_2(OH)_2$ and CrO_2 [2], migrate into the porous cathode and react with the surface of the cathode.

Chromium poisoning is predominately seen in lanthanum strontium manganese oxide (LSM) cathodes, which have traditionally been the cathode material of choice in SOFCs. Recent studies have found that in the LSM cathode chromium species can drastically decrease the performance of the fuel cell over relatively short periods of time. For an SOFC operated at 800 °C with a current density of 250 mA cm^{-2}, a decrease in cell voltage of 5% per 1000 h has been seen and at higher current densities decreases of 20% per 1000 h have been seen [3].

Investigations of chromium deposition on the LSM cathode have shown that in a poisoned cell chromium is predominately deposited in the electrochemically active area of the cathode directly next to the electrolyte interface [4–6]. Several different mechanisms of chromium poisoning in LSM have been proposed over the years based on different chemical and electrochemical reactions [5]. Chemical reactions have been shown to be possible between LSM and chromium at the SOFC operating temperatures but do not show preferential chromium deposition in the electrochemically active area [6,7]. The more likely reaction mechanism is related to the electrochemical reactions and voltage potential of

* Corresponding author at: Pacific Northwest National Laboratory, Computational Science and Mathematics Division, P.O. Box 999, Richland, WA 99352, USA. Tel.: +1 206 528 3206; fax: +1 206 528 3557.
E-mail addresses: emily.ryan@pnl.gov, eryan@alumni.cmu.edu (E.M. Ryan), alexandre.tartakovsky@pnl.gov (A.M. Tartakovsky), kp.recknagle@pnl.gov (K.P. Recknagle), moe.khaleel@pnl.gov (M.A. Khaleel), dean@ecf.utoronto.ca (C. Amon).

0378-7753/$ – see front matter © 2010 Elsevier B.V. All rights reserved.
doi:10.1016/j.jpowsour.2010.06.030

the SOFC. Two different reaction mechanisms have been proposed to explain how chromium reacts with the electrochemically active cathode. The first mechanism proposes that chromium reacts with the free electrons and oxygen vacancies on the cathode surface via reactions such as [2,4]

$$2CrO_2(OH)_2(g) + 6e^- + 3V_O^{\bullet\bullet} \rightarrow Cr_2O_3(s) + 3O_O^x + 2H_2O \quad (1)$$

$$2CrO_2(g) + 6e^- + 3V_O^{\bullet\bullet} \rightarrow Cr_2O_3(s) + 3O_O^x \quad (2)$$

In reactions (1) and (2) as the current density increases the available electrons (e^-) and oxygen vacancies ($V_O^{\bullet\bullet}$) will also increase allowing for increased chromium deposition on the cathode surface due to increased available adsorption sites. The increased chromium deposition in turn reduces the sites available for oxygen to adsorb and electrochemically react decreasing the output voltage of the SOFC. The second electrochemically related reaction mechanism suggests a chemical reaction between chromium and manganese ions formed under the voltage potential in the LSM, which act as nucleation sites for chromium to form Cr_2O_3 and a manganese spinel [8],

$$Mn^{2+}(s) + CrO_3(g) \rightarrow Cr\text{–}Mn\text{–}O(\text{nuclei}) \quad (3)$$

$$Cr\text{–}Mn\text{–}O(\text{nuclei}) + CrO_3(g) \rightarrow Cr_2O_3(s) \quad (4)$$

$$Cr_2O_3(s) + CrO_3(g) + Mn^{2+}(s) \rightarrow (Cr, Mn)O_4(s) \quad (5)$$

The Cr_2O_3 and spinel formed on the LSM block the migration of oxygen to the triple phase boundaries reducing the oxygen available for the electrochemical reactions.

Both electrochemically related reaction mechanisms involve the adsorption of chromium species to the cathode surface, which blocks oxygen from adsorbing to the surface and/or diffusing to the triple phase boundaries of the cathode. In this paper we present a pore-scale reactive transport model of chromium and oxygen in an SOFC cathode to investigate the reaction mechanisms of chromium poisoning. We consider the transport of oxygen and chromium within the porous cathode structure and the surface reactions of oxygen and chromium with the surface. In our model we represent the surface reactions as a competitive adsorption process between oxygen and chromium. Although the exact mechanisms of chromium poisoning are not known, it is clear that chromium adsorbs to the surface of the cathode where it may then react further with manganese or other species in the cathode. Likewise, the reaction steps of oxygen reduction in the cathode are an area of continued research but oxygen also adsorbs to the LSM surface before being reduced [9–11].

Past research on chromium poisoning has focused on experimental efforts to characterize chromium's effects on the overall performance of the fuel cell [4,12–15] and different strategies to decrease the amount of chromium volatized in the air channel [16–18]. Research on the fundamental mechanisms of chromium poisoning has been limited with only a handful of studies considering the transport and reaction mechanisms of chromium in the cathode [5,7,8,14,19,20]. Understanding the details of degradation issues such as chromium poisoning can help researchers to better understand the physics of the problem and can aid in the design of mitigation strategies for chromium poisoning.

In this paper we present a multi-scale modeling approach to investigate the reactive transport of oxygen and chromium in the cathode. The central part of this approach is a pore-scale smoothed particle hydrodynamics (SPH) model of chromium reactive transport in a small section of the cathode, which is modeled as a discrete porous microstructure. The multi-scale approach also includes a cell level (continuum-scale) model of the cathode, air channel and current collector. The cell level model is used to determine the boundary conditions for the pore-scale model based on typical SOFC operating conditions. The cell level model, based on the commercial computational fluid dynamics software Fluent, does not consider the reactions of oxygen and chromium in the cathode, and only includes the transport of species in the air channel and cathode, and the vaporization of chromium from the current collector walls.

Past models of reactive transport within the SOFC electrodes have focused on cell level, continuum-scale models, such as the Dusty Gas Model [21–23]. In these models the electrode microstructure is not explicitly resolved and instead it is accounted for via effective parameters. The effective parameters, such as the effective diffusion coefficient and permeability, are based on the average structural properties of the electrodes and the assumption of a homogeneous microstructure. In pore-scale models the electrode microstructure is discretely resolved negating the need for effective parameters and allowing for heterogeneous microstructures to be modeled.

The remaining of the paper is divided into six sections which discuss the reactive transport model of the cathode and parametric studies of chromium poisoning in the cathode: Section 2 describes the pore-scale reactive transport equations, Section 3 outlines the numerical implementation of the pore-scale model, Section 4 discusses the cell level model and results which are used as boundary conditions in the pore-scale model, Section 5 presents parametric studies of chromium in the cathode via the pore-scale model of the cathode and Section 6 discusses the conclusions drawn from this work.

2. Pore-scale reactive transport equations

In reactive transport problems a porous medium can be treated explicitly as a combination of grains and voids (pores) or as a continuum. The continuum (Darcy) description of reactive transport is computationally more efficient but relies heavily on phenomenological descriptions of the reaction processes and requires knowledge of effective parameters describing continuum structural and transport properties of the porous media, such as porosity, tortuosity, average grain radii, effective diffusion coefficient, effective surface area and effective reaction rates. As a result, the accuracy of continuum models cannot be assessed *a priori*.

In our model we use a discrete representation of the SOFC cathode to model the system on the pore-scale. In a discrete (pore-scale) model, the computational domain Ω representing the cathode consists of two non-overlapping sub-domains: $\Omega \in \Omega_P \cup \Omega_S$, where Ω_S is the solid sub-domain occupied by the cathode material (assumed here to be impermeable for the oxygen and chromium) and Ω_P is the pore sub-domain. At the surface of the cathode Γ, $\Gamma \in \Omega_P \cap \Omega_S$, oxygen and chromium competitively adsorb as discussed in Section 1.

The section of the cathode which is included in the pore-scale model is shown in Fig. 1. A schematic of the full SOFC cell, including the pore-scale domain, is shown in Fig. 2. The pore-scale simulation domain is a 2D representation of a porous cathode where the domain consists of solid circular grains representing the cathode (Ω_S) surrounded by the pore space (Ω_P). Although an idealized porous microstructure is modeled, the macroscopic properties of the microstructure are consistent with the macroscopic properties of a typical SOFC cathode. Namely, the average grain radii (1 μm), porosity (0.42) and thickness (45 μm) are within the accepted ranges of the cathode [4,24,25].

The simulation domain is bounded by the electrolyte at B_{EL}, the current collector at B_{CC} and the air channel at B_{AC}. The cathode domain is divided into two regions, the non-electrochemically active cathode, $\boldsymbol{R}_{CA}$, and the electrochemically active cathode, $\boldsymbol{R}_{EC}$. In $\boldsymbol{R}_{EC}$ oxygen is removed from the system due to the electrochem-

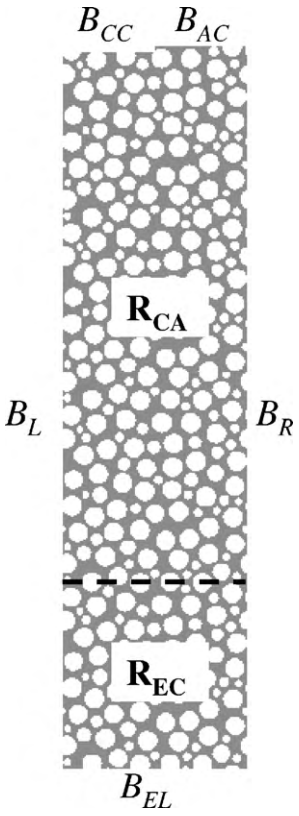

Fig. 1. The 2D pore-scale cathode domain, where the cathode material is represented by the circular grains (white) and is surrounded by the gas (grey). The external boundaries of the pore-scale domain are labeled as well as the non-electrochemically active region (R_{CA}) and the electrochemically active region (R_{EC}).

ical reactions of the SOFC. $\boldsymbol{R}_{EC}$ is assumed to be the region within ~10 μm of the electrolyte. In the cathode the electrochemical reactions are assumed to occur within 5–10 μm of the cathode-electrolyte interface [26].

The pore-scale model of the cathode is used to investigate chromium poisoning by considering the transport and reactions of chromium in the cathode. In general, transport of chemical species in porous media is a result of both advection and molecular diffusion and both these mechanisms are considered in the pore-scale model. In Appendix A we study the air flow in the cathode and show that the air velocity in the cathode is very small and the advection of gaseous species is negligible when compared to gas diffusion. Because of this, advection is neglected in our parametric studies of chromium poisoning in the cathode (Section 5). Since advection is not a significant transport mechanism, only the diffusion and reactions of oxygen and chromium are modeled in our pore-scale model and are laid out in this section. Additionally, the different diffusion mechanisms possible in the cathode are discussed in Section 2.1. Due to the average pore size in the cathode, both molecular and Knudsen diffusion are included in the pore-scale model.

2.1. Diffusion

In the SOFC cathode, diffusion of species can take place in both the gas (Ω_P) and on the surface of the cathode (Γ). Since gas diffusion is much faster than surface diffusion [10] only gas diffusion is considered in the pore-scale model and is described by Fick's law of diffusion, $J(\vec{x}) = -D(\vec{x})\nabla c^a(\vec{x})$, where J is the diffusive flux, c^a is the concentration of species a (a = O, Cr) and D is the diffusion coefficient.

In the pore sub-domain the diffusion of species is described by:

$$\frac{\partial c^a(\vec{x},t)}{\partial t} = \nabla\cdot(D(\vec{x})\nabla c^a(\vec{x},t)) \quad \vec{x}\in\Omega_P \tag{6}$$

In the cathode, both molecular and Knudsen diffusion of gaseous species can be important [27]. SOFC cathodes typically have an average pore radii of ~ 1 μm [24,25], which places diffusion in the transition region between the molecular and Knudsen diffusion regimes. Molecular diffusion is the diffusion of species due to the molecule–molecule interactions; while Knudsen diffusion is due to molecule–wall interactions [28]. The transition region applies to conditions where the Knudsen number is between 0.01 and 1 [29]. Based on the average pore radii of the cathode and a typical SOFC operating temperature of 1073 K, the average Knudsen number in the cathode is 0.13 which falls in the transition region.

Continuum-scale models of diffusion in the cathode use an effective diffusion coefficient to account for both molecular and Knudsen diffusion. The effective coefficient is usually given by the Bosanquet formula [30–32]. In a pore-scale model, the molecular diffusion coefficient can be used to describe diffusion in larger pores while the Knudsen diffusion coefficient should be used to model diffusion in smaller pores. This could be accomplished by dividing the domain into zones depending on pore radii and applying the appropriate diffusion coefficients to the different regions.

The molecular diffusion coefficient, D_{ij}, can be calculated from the Chapman–Enskog Theory [33],

$$D_{ij} = \frac{1.86\cdot 10^{-3}T^{2/3}\left(\frac{1}{M_i}+\frac{1}{M_j}\right)^{1/2}}{P\sigma_{ij}^2\Omega} \tag{7}$$

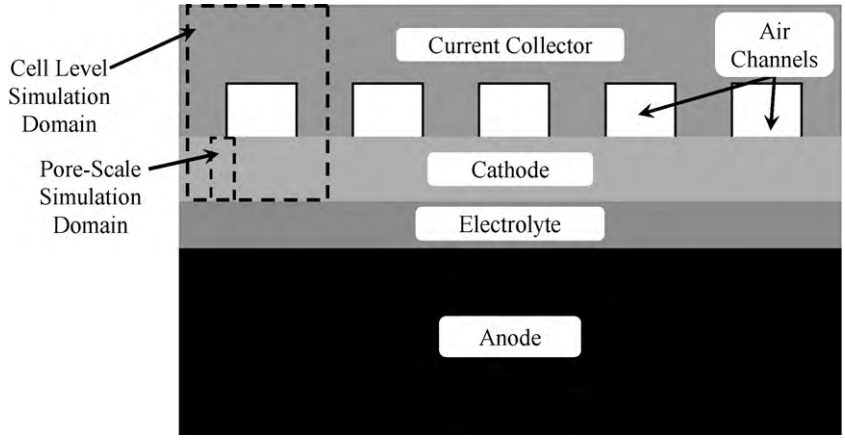

Fig. 2. SOFC schematic (not to scale) showing the pore-scale simulation domain and the cell level simulation domain. The pore-scale simulation domain is detailed in Fig. 1.

Table 1
Species transport and reaction parameters.

Species	Diffusion coefficients		Molecular radii [40]	Adsorption coefficient [41]	Desorption coefficient [41]
	Molecular	Knudsen			
Oxygen	9.35E−05 $m^2\,s^{-1}$	5.6E−04 $m^2\,s^{-1}$	1.4E−4 μm	3.95E−1 $m\,s^{-1}$	1.44E−3 $kg\,m^{-2}\,s^{-1}$
Chromium	9.35E−05 $m^2\,s^{-1}$	5.9E−04 $m^2\,s^{-1}$	1.3E−4 μm	–	–

where T is temperature, P is pressure, M_i is the molecular mass of species i, and σ_{ij} and Ω are molecular properties of the species which can be found in [33] for common gaseous species.

The Knudsen diffusion coefficient can be defined by, [28]

$$D_i^K = \frac{d}{3}\left(\frac{8RT}{\pi M_i}\right)^{1/2} \tag{8}$$

where d is the mean pore diameter and R is the universal gas constant.

Based on the typical operating conditions of an SOFC cathode (1073 K, 1 atm) and the molecular masses of oxygen and chromium, the molecular and Knudsen diffusion coefficients in the cathode will be of roughly the same order of magnitude, as summarized in Table 1. For simplicity, in the model presented here we use a single diffusion coefficient assumed to be equal to the molecular diffusion coefficient to model pore-scale diffusion. The Knudsen and molecular diffusion coefficient calculations contain a number of estimated parameters (such as σ_{ij} and Ω) and assume some idealizations, such as cylindrical pores in the Knudsen equation (8), which cause uncertainty in the calculations. Since the main focus of this paper is to study the distribution of chromium in the cathode we chose not to model the two different diffusion mechanisms in detail. Additionally in Section 5 we show that the reaction rates have a greater effect on chromium poisoning and the distribution of chromium in the cathode than the diffusion coefficient.

2.2. Competitive adsorption

The reactions of oxygen and chromium on the cathode surface are described by a competitive adsorption process, where both oxygen and chromium species are competing for the same adsorption sites on the cathode surface.

Competitive adsorption is described in the pore-scale model by the boundary condition of the diffusion equation (6) at the solid grains,

$$D(\vec{x}_s)\nabla c^a(\vec{x}_s)\cdot\vec{n} = R_S^a(\vec{x}_s,t) \quad \vec{x}_s \in \Gamma \tag{9}$$

where $\vec{x}_s$ is a point on the cathode surface Γ, $\vec{n}$ is the normal to Γ and R_S^a is the surface reaction describing a competitive adsorption reaction according to the Langmuir model [34],

$$R_S^a(\vec{x}_s,t) = k_a^+ c^a(\vec{x}_s,t)[1-\theta^a(\vec{x}_s,t)-\theta^b(\vec{x}_s,t)]^g - k_a^-(\theta^a(\vec{x}_s,t))^g \quad \vec{x}_s \in \Gamma \tag{10}$$

where θ^a is the normalized surface concentration of species a (a = O, Cr), k_a^+ and k_a^- are the adsorption and desorption rate coefficients, respectively, and g is the number of adsorption sites needed by each species. The Langmuir adsorption model assumes monolayer adsorption on the surface of the cathode and constant reaction rates with coverage. The model is commonly used in reactive transport models [35–37] and has been used in previous models of reactive transport in SOFCs [38,39].

In our model we consider the competitive adsorption of oxygen to be dissociative where diatomic oxygen in the gas adsorbs to two adsorption sites on the cathode surface; while chromium adsorption is described by Eqs. (1) and (2) which require three adsorption sites (oxygen vacancies) to adsorb to the cathode. From Eq. (10), the reaction terms for oxygen and chromium can be written as,

$$R_S^{\mathrm{O}}(\vec{x}_s,t) = k_{\mathrm{O}}^+ c^{\mathrm{O}}(\vec{x}_s,t)\left[1-\theta^{\mathrm{O}}(\vec{x}_s,t)-\theta^{\mathrm{Cr}}(\vec{x}_s,t)\right]^2 - k_{\mathrm{O}}^-(\theta^{\mathrm{O}}(\vec{x}_s,t))^2 \quad \vec{x}_s \in \Gamma \tag{11}$$

$$R_S^{\mathrm{Cr}}(\vec{x}_s,t) = k_{\mathrm{Cr}}^+ c^{\mathrm{Cr}}(\vec{x}_s,t)[1-\theta^{\mathrm{Cr}}(\vec{x}_s,t)-\theta^{\mathrm{O}}(\vec{x}_s,t)]^3 - k_{\mathrm{Cr}}^-(\theta^{\mathrm{Cr}}(\vec{x}_s,t))^3 \quad \vec{x}_s \in \Gamma \tag{12}$$

In the model the normalized surface concentrations of oxygen and chromium are both normalized by the same maximum surface concentration, $\theta^a = s^a/s_{\max}$. The maximum surface concentration, s_{max}, can be approximated by the inverse of the square of the molecular diameter of the adsorbed species [34,40]. Based on the molecular radii of oxygen and $CrO_2(OH)_2$, which we consider the form of chromium in the model, both species have the same radii, Table 1.

The adsorption (k_a^+) and desorption (k_a^-) coefficients, Table 1, for oxygen are taken from [41], which investigated the adsorption of oxygen on an LSM cathode. The adsorption and desorption coefficients for chromium on LSM are unknown and to the best of the authors' knowledge have not been studied. In Section 5, the chromium reaction rates are considered in the parametric studies to investigate their effect on chromium poisoning.

Since the cathode is assumed to be an impermeable solid, from mass conservation considerations the change in surface concentration (s^a) is,

$$\frac{ds^a}{dt} = R_S^a(\vec{x}_s,t) \quad \vec{x}_s \in \Gamma \tag{13}$$

An accurate numerical treatment of the reactive boundary condition, Eq. (9), in domains with complex geometries (such as the cathode's pore domain) presents a significant challenge for any numerical method. A smoothed particle hydrodynamics (SPH) solution of this diffusion-reaction problem can be significantly simplified by using the continuum surface reaction (CSR) model [42] that replaces the boundary Γ with a diffuse interface. The CSR model replaces the original diffusion equation subject to the non-homogeneous boundary condition (9) with the diffusion-reaction equation

$$\frac{\partial c^a(\vec{x},t)}{\partial t} = \nabla\cdot(D(\vec{x})\nabla c^a(\vec{x},t)) - R_V^a(\vec{x},t) \quad \vec{x}\in\Omega_P \tag{14}$$

subject to the homogeneous Neumann boundary condition

$$\vec{n}\cdot D\nabla c^a(\vec{x}_s,t) = 0 \quad \vec{x}_s \in \Gamma \tag{15}$$

where R_V^a is the volumetric source term due to competitive adsorption.

The CSR model accomplishes the transformation to Eqs. (14) and (15) by employing a characteristic function (φ), which has a unique value on either side of the surface. The details of the CSR model are discussed in [42,43], and the pore-scale transport model with competitive adsorption reactions in porous media is validated and compared to a Darcy-scale model in [43]. Using the CSR model, the

diffusion-reaction equation (14) can be defined as [43],

$$\frac{\partial c^a(\vec{x},t)}{\partial t} = \nabla\cdot(D(\vec{x})\nabla c^a(\vec{x},t)) - \int_{\Omega_S} \tilde{R}_S^a(\vec{x},\vec{x}',t)\left(\vec{n}(\vec{x})+\vec{n}(\vec{x}')\right) \times \left(\varphi(\vec{x}')-\varphi(\vec{x})\right)\nabla_{\vec{x}} W(\vec{x}'-\vec{x},h_r)d\vec{x}' \quad \vec{x}\in\Omega_P, \tag{16}$$

where φ is the characteristic function, W is the smoothed particle hydrodynamics (SPH) smoothing function, which is discussed in Section 3, and $\tilde{R}_S^a$ is given by [43],

$$\tilde{R}_S^a(\vec{x},\vec{x}',t) = k_a^+ c^a(\vec{x},t)\left[1-\tilde{\theta}^a(\vec{x}',t)-\tilde{\theta}^b(\vec{x}',t)\right]^g - k_a^-(\tilde{\theta}^a(\vec{x}',t))^g \quad \vec{x}\in\Omega_P,\ \vec{x}'\in\Omega_S. \tag{17}$$

In Eq. (17), θ^a, which is defined on Γ, has been replaced with $\tilde{\theta}^a$ which is defined throughout the solid side of the diffuse interface as

$$\tilde{\theta}^a(\vec{x},t) = \frac{\tilde{s}^a(\vec{x},t)}{\tilde{s}^a_{\max}(\vec{x})} \quad \vec{x}\in\Omega_S \tag{18}$$

where the rate of change of the surface concentration, $\tilde{s}^a$, due to the surface reactions is written in CSR form as [43],

$$\frac{d\tilde{s}^a(\vec{x},t)}{dt} = \int_{\Omega_P} \tilde{R}_S^a(\vec{x},\vec{x}',t)(\vec{n}(\vec{x})+\vec{n}(\vec{x}'))(\varphi(\vec{x}') - \varphi(\vec{x}))\nabla_{\vec{x}} W(\vec{x}'-\vec{x},h_r)d\vec{x}' \quad \vec{x}\in\Omega_S, \tag{19}$$

and $\tilde{s}^a_{\max}$ is written as,

$$\tilde{s}^a_{\max}(\vec{x}) = s^a_{\max}\int_{\Omega_P} (\vec{n}(\vec{x})+\vec{n}(\vec{x}'))(\varphi(\vec{x}') - \varphi(\vec{x}))\nabla_{\vec{x}} W(\vec{x}'-\vec{x},h_r)d\vec{x}' \quad \vec{x}\in\Omega_S \tag{20}$$

where s^a and $s^a_{\max}$, which were defined on the surface, have been replaced with volumetric surface concentrations $\tilde{s}^a$ and $\tilde{s}^a_{\max}$ defined over the diffuse interface.

Now the complete set of governing equations for the diffusion and reactions of oxygen and chromium in the cathode is given by,

$$\frac{\partial c^{\mathrm{O}}(\vec{x},t)}{\partial t} = \nabla\cdot(D(\vec{x})\nabla c^{\mathrm{O}}(\vec{x},t)) - \int_{\Omega_S} \tilde{R}_S^{\mathrm{O}}(\vec{x},\vec{x}',t)(\vec{n}(\vec{x})+\vec{n}(\vec{x}'))(\varphi(\vec{x}') - \varphi(\vec{x}))\nabla_{\vec{x}} W(\vec{x}'-\vec{x},h_r)d\vec{x}' \quad \vec{x}\in\Omega_P \tag{21}$$

$$\frac{\partial c^{\mathrm{Cr}}(\vec{x},t)}{\partial t} = \nabla\cdot(D(\vec{x})\nabla c^{\mathrm{Cr}}(\vec{x},t)) - \int_{\Omega_S} \tilde{R}_S^{\mathrm{Cr}}(\vec{x},\vec{x}',t)(\vec{n}(\vec{x})+\vec{n}(\vec{x}'))(\varphi(\vec{x}') - \varphi(\vec{x}))\nabla_{\vec{x}} W(\vec{x}'-\vec{x},h_r)d\vec{x}' \quad \vec{x}\in\Omega_P \tag{22}$$

$$\frac{d\tilde{s}^{\mathrm{O}}(\vec{x},t)}{dt} = \int_{\Omega_P} \tilde{R}_S^{\mathrm{O}}(\vec{x},\vec{x}',t)(\vec{n}(\vec{x})+\vec{n}(\vec{x}'))(\varphi(\vec{x}') - \varphi(\vec{x}))\nabla_{\vec{x}} W(\vec{x}'-\vec{x},h_r)d\vec{x}' \quad \vec{x}\in\Omega_S \tag{23}$$

$$\frac{d\tilde{s}^{\mathrm{Cr}}(\vec{x},t)}{dt} = \int_{\Omega_P} \tilde{R}_S^{\mathrm{Cr}}(\vec{x},\vec{x}',t)(\vec{n}(\vec{x})+\vec{n}(\vec{x}'))(\varphi(\vec{x}') - \varphi(\vec{x}))\nabla_{\vec{x}} W(\vec{x}'-\vec{x},h_r)d\vec{x}' \quad \vec{x}\in\Omega_S \tag{24}$$

where $\tilde{R}_S^{\mathrm{O}}$ and $\tilde{R}_S^{\mathrm{Cr}}$ are defined by

$$\tilde{R}_S^{\mathrm{O}}(\vec{x},\vec{x}',t) = k_{\mathrm{O}}^+ c^{\mathrm{O}}(\vec{x},t)\left[1-\tilde{\theta}^{\mathrm{O}}(\vec{x}',t)-\tilde{\theta}^{\mathrm{Cr}}(\vec{x}',t)\right]^2 - k_{\mathrm{O}}^-(\tilde{\theta}^{\mathrm{O}}(\vec{x}',t))^2 \quad \vec{x}\in\Omega_P, \vec{x}'\in\Omega_S \tag{25}$$

$$\tilde{R}_S^{\mathrm{Cr}}(\vec{x},\vec{x}',t) = k_{\mathrm{Cr}}^+ c^{\mathrm{Cr}}(\vec{x},t)\left[1-\tilde{\theta}^{\mathrm{Cr}}(\vec{x}',t)-\tilde{\theta}^{\mathrm{O}}(\vec{x}',t)\right]^3 - k_{\mathrm{Cr}}^-(\tilde{\theta}^{\mathrm{Cr}}(\vec{x}',t))^3 \quad \vec{x}\in\Omega_P,\ \vec{x}'\in\Omega_S \tag{26}$$

Eqs. (21)–(26) constitute the complete set of governing equations for the pore-scale cathode model presented in Section 5.

3. Pore-scale numerical implementation

The smoothed particle hydrodynamics (SPH) method is used to discretize the pore-scale reactive transport equations, given in Section 2. SPH is a grid free method for solving partial differential equations in a Lagrangian framework. SPH discretizes the system with a set of particles used as interpolation points to solve the governing equations of the system. The method was originally developed to model astronomical systems [44,45], and in recent years has been applied to the diffusion, advection and reactions of chemical and biological species in porous and fractured media [46–49].

SPH is based on the concept that a continuous field, A, can be approximated by an integral interpolant [50],

$$A_s(\vec{x}) = \int_{\Omega_P\cup\Omega_S} A(\vec{x}')W(\vec{x}'-\vec{x},h)d\vec{x}' \quad \vec{x}\in\Omega_P\cup\Omega_S \tag{27}$$

where A_s is the approximation of A, W is the SPH smoothing function with a support length of h and the integration is performed over the entire domain of A. In SPH the smoothing function is chosen such that it is n-times differentiable, normalized over the volume, has a compact support h ($W(|x|>h)=0$) and tends towards the delta function as $h\to 0$. When W is the delta function Eq. (27) reproduces A exactly [50].

In the SPH method all domains (pore and solid sub-domains in our model) are discretized with a set of particles and the integral, Eq. (27), is approximated as the summation over a discrete number of particles where the value of A is know at each point,

$$A_s(\vec{x}) = \sum_i \frac{A_i}{d_i} W(\vec{x}-\vec{x}_i,h) \quad \vec{x}\in\Omega_P\cup\Omega_S \tag{28}$$

where $\vec{x}_i$ is the position of particle i, $A_i = A(\vec{x}_i)$, $d_i = \rho_i/m_i$ is the particle number density, ρ_i is the fluid density and m_i is the mass of particle i [50]. Due to the compact support of W only particles within distance h of x need to be included in (28) which greatly reduces the computational cost of the SPH method.

The SPH discretization scheme is used to discretize the pore-scale governing equations, Eqs. (21)–(24) [43]. In the pore-scale model of the cathode, the domain is discretized with two sets of particles: Ω_S is discretized with "solid" particles and the gas phase occupying Ω_P is discretized with "gas" particles. The equations for the gaseous species can be discretized as:

$$\frac{\partial c_i^{\mathrm{O}}}{\partial t} = \frac{1}{m_i}\sum_{j\in\text{gas}} \frac{D_i(m_i d_i + m_j d_j)}{d_i d_j}(c_i^{\mathrm{O}} - c_j^{\mathrm{O}})\frac{\vec{x}_{ij}}{\vec{x}_{ij}^2}\nabla_i W(\vec{x}_{ij},h) - \sum_{k\in\text{solid}}\left[k_{\mathrm{O}}^+ c_i^{\mathrm{O}}\left[1-\tilde{\theta}_k^{\mathrm{O}}-\tilde{\theta}_k^{\mathrm{Cr}}\right]^2 - k_{\mathrm{O}}^-(\tilde{\theta}_k^{\mathrm{O}})^2\right] \times \frac{2(\varphi_i-\varphi_k)(\vec{n}_i+\vec{n}_k)}{d_k+d_i}\nabla_i W(\vec{x}_{ik},h_r) \quad i\in\text{gas particles} \tag{29}$$

$$\frac{\partial c_i^{\mathrm{Cr}}}{\partial t} = \frac{1}{m_i}\sum_{j\in\text{gas}} \frac{D_i(m_i d_i + m_j d_j)}{d_i d_j}\left(c_i^{\mathrm{Cr}} - c_j^{\mathrm{Cr}}\right)\frac{\vec{x}_{ij}}{\vec{x}_{ij}^2}\nabla_i W(\vec{x}_{ij},h) - \sum_{k\in\text{solid}}\left[k_{\mathrm{Cr}}^+ c_i^{\mathrm{Cr}}\left[1-\tilde{\theta}_k^{\mathrm{Cr}}-\tilde{\theta}_k^{\mathrm{O}}\right]^3 - k_{\mathrm{Cr}}^-\left(\tilde{\theta}_k^{\mathrm{Cr}}\right)^3\right]$$

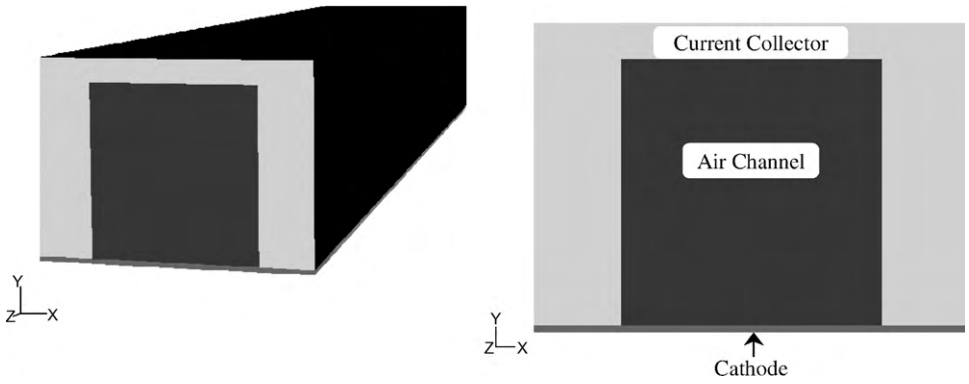

Fig. 3. Cell level 3D Geometry of the cathode air channel, current collector and cathode.

$$\times \frac{2(\varphi_i - \varphi_k)\left(\vec{n}_i + \vec{n}_k\right)}{d_k + d_i} \nabla_i W(\vec{x}_{ik}, h_r) \quad i \in \text{gas particles} \quad (30)$$

where D_i is the gas diffusion coefficient, c_i^a is the gas concentration of species a, φ_i is the characteristic function of particle i, which is used in the CSR model, and $\tilde{\theta}_k^a$ is the normalized surface concentration of species a of particle k.

The equations for the concentration of surface species take the form:

$$\frac{d\tilde{s}_k^{\mathrm{O}}}{dt} = \sum_{i \in \text{gas}} \left[k_{\mathrm{O}}^{+} c_i^{\mathrm{O}} \left[1 - \tilde{\theta}_k^{\mathrm{O}} - \tilde{\theta}_k^{\mathrm{Cr}}\right]^2 - k_{O}^{-} \left(\tilde{\theta}_k^{\mathrm{O}}\right)^2 \right]$$

$$\times \frac{2(\varphi_k - \varphi_i)(\vec{n}_i + \vec{n}_k)}{d_i + d_k} \nabla_k W(\vec{x}_{ki}, h_r) \quad k \in \text{solid particles} \quad (31)$$

$$\frac{d\tilde{s}_k^{\mathrm{Cr}}}{dt} = \sum_{i \in \text{gas}} \left[k_{\mathrm{Cr}}^{+} c_i^{\mathrm{Cr}} \left[1 - \tilde{\theta}_k^{\mathrm{Cr}} - \tilde{\theta}_k^{\mathrm{O}}\right]^3 - k_{\mathrm{Cr}}^{-} \left(\tilde{\theta}_k^{\mathrm{Cr}}\right)^3 \right]$$

$$\times \frac{2(\varphi_k - \varphi_i)(\vec{n}_i + \vec{n}_k)}{d_i + d_k} \nabla_k W(\vec{x}_{ki}, h_r) \quad k \in \text{solid particles} \quad (32)$$

where $\tilde{s}_k^a$ is the volumetric surface concentration of species a of particle k.

The 2D pore-scale model of the cathode presented in this paper simulates the reactive transport by solving Eqs. (29)–(32). In Section 5, the pore-scale equations are simulated for a 2D porous domain, Fig. 1. The 2D domain consists of the pore space and the solid cathode which is made up of randomly placed circular grains having a porosity of 0.42, which is similar to that of SOFC cathodes (~0.3–0.4). The solid grains in the domain have an average radius of 1 μm and the domain is roughly 45 μm thick. Modeling gas transport in the 2D domain requires connectivity of the pore space in the cathode. By necessity this requires the cathode solid sub-domain to be discontinuous making it impossible to model the transport of species through the cathode due to surface diffusion. However, as mentioned earlier, the surface diffusion coefficient of oxygen in the cathode is much smaller than the gas diffusion coefficient and so surface diffusion should not be a significant transport mechanism in the cathode [10]. Work is currently being done to expand the model to 3D to investigate the effects of surface diffusion and real cathode microstructures on reactive transport.

In Section 5, Eqs. (29)–(32) are solved to investigate the effects of reaction rate, current density and the vaporization rate of chromium from the current collector on chromium adsorption and distribution in the cathode.

4. 3D cell level model of a SOFC

The commercial computational fluid dynamics software Fluent is used to model the 3D air flow and chromium transport in the air channel and cathode in a SOFC at the cell level. In this model the porous material of the cathode is treated as a continuum and transport in the cathode is described by the Darcy-scale diffusion equation. The results of the cell level model are used as boundary and initial conditions for the pore sub-domain in the pore-scale model. Due to the computational expense of a detailed pore-scale reactive transport model only a small section of the cathode can be modeled at the pore-scale and a cell level model of the SOFC is required to establish the boundary conditions at the external boundaries of the pore-scale model. The cell level model of the SOFC provides the species boundary conditions along the boundaries B_{AC}, B_L and B_R, Fig. 1. The cell level model includes the advection and diffusion of air and chromium in the air channel, vaporization of chromium from the current collector walls and species transport in the cathode. The cell level model does not resolve the detailed cathode microstructure nor does it include the reactions of chromium and oxygen in the cathode.

The geometry of the cell level model consists of a symmetric section of the cathode and air channel as shown in Fig. 3. The dimensions and operating conditions of the cell level model are typical of SOFCs [4] and are shown in Table 2. The microstructural parameters of the cathode which are necessary for the Darcy-scale model are taken from literature and are shown in Table 2 [21,25,51].

The vaporization of chromium from the current collector is modeled as a source term in the cell level model. The vaporization rate of chromium from the current collector is taken from experimental vaporization rates of chromium collected at Pacific Northwest National Laboratory (PNNL) which are in line with published rates [18,52]. Once chromium is introduced to the air channel it is transported by advection and multi-component diffusion through the air channel to the cathode. Although the reactions of oxygen and chromium are not included in the cell level model, the consumption of oxygen due to the electrochemical reactions is included as a prescribed flux of oxygen out of the cathode at the cathode-electrolyte

Table 2
Cell level model parameters.

Cathode thickness	50 μm
Air channel	$1.6 \times 1.6 \times 16\,\mathrm{mm}^3$
Current collector ribs thickness	0.85 mm
Air flow	160 sccm
Temperature	1073 K
Pressure	1 atm
Current density	$0.4\,\mathrm{A\,cm^{-2}}$
Porosity	0.4
Permeability	$1\mathrm{E}{-14}\,\mathrm{m}^2$

boundary. The oxygen flux is calculated from the current density of the SOFC as,

$$\dot{m}_{O_2} = \frac{M_{O_2} j}{4F} \tag{33}$$

where F is Faraday's constant (96,400 C mol^{-1}), M_{O_2} is the molecular weight of oxygen and j is the current density [53].

Simulations were performed with the cell level model to simulate species transport in the SOFC for various air channel flow rates and chromium vaporization rates. As shown in Fig. 4a the concentration of chromium at the air channel–cathode interface decreases with increasing air channel flow rate as the advection of chromium, in the direction of flow, becomes the dominant transport mechanism. As the vaporization of chromium at the current collector walls is increased the chromium concentration at the air channel–cathode interface increases, Fig. 4b. The molar concentrations of chromium species predicted by the cell level model in the air channel are comparable with the partial pressures found in the thermodynamic studies of chromium in the air channel by Hilpert et al. [2]. They found the partial pressure of chromium in air to be in the range of 10^{-2} to 10^{-4} Pa (10^{-9} to 10^{-12} kmol m^{-3}) depending on the operating temperature and humidity of the air in the model.

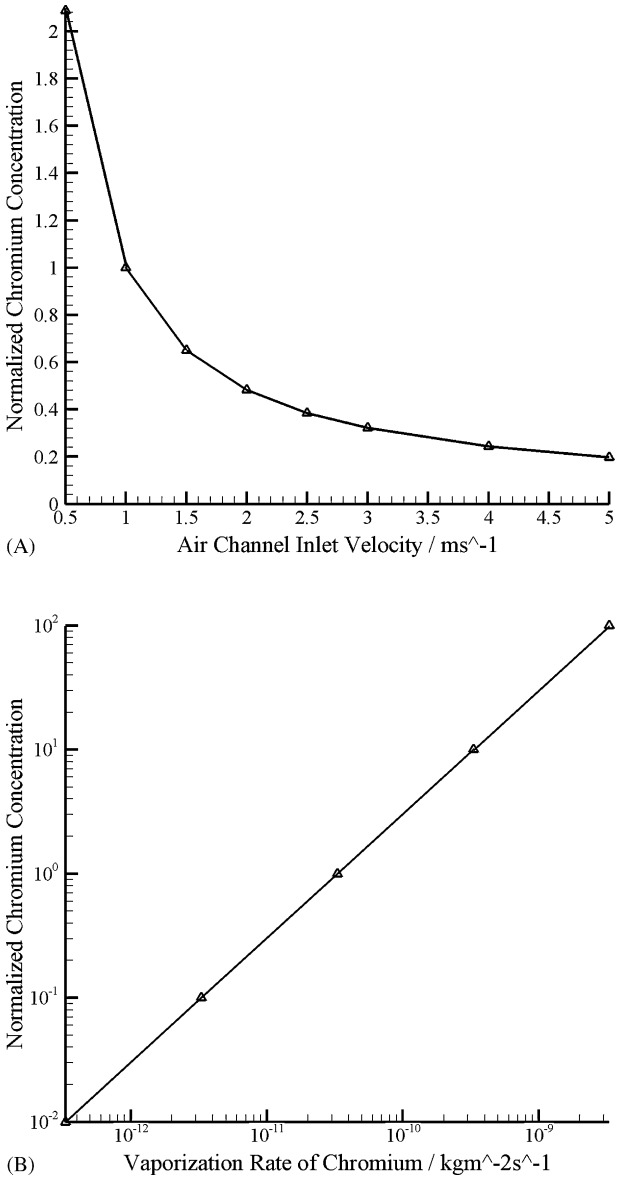

Fig. 4. Results of cell level parametric study of air channel velocity (a) and chromium vaporization (b) effects on the concentration of chromium at the air channel-cathode interface. The chromium concentration is normalized by the baseline cell level conditions.

Table 3
Average molar concentration [kmol m^{-3}] of oxygen and chromium at the air channel-cathode interface.

Cr	4.39E−12
O_2	2.12E−03

For the pore-scale model of the cathode, the species concentrations shown in Table 3 are used as baseline boundary conditions at B_{AC}. For the boundary conditions along B_L and B_R in the pore-scale model a no flux boundary condition is applied. The flux of species along B_L and B_R were investigated in the cell level model and were found to be uniform throughout the cathode and on the order of 10^{-11} kg m^{-2} which is insignificant when compared to the gas diffusion and surface reactions in the pore-scale model.

5. Pore-scale model of chromium poisoning in the cathode

5.1. Simulation setup and boundary conditions

The 2D section of the cathode shown in Fig. 1 was modeled using the SPH pore-scale reactive transport model outlined in Section 3 to investigate the reaction mechanisms of chromium poisoning and the effect of different parameters on chromium poisoning. Five parameters were investigated: the magnitude of the chromium reaction rates, the oxygen consumption due to the electrochemical reactions, the chromium reaction rate as a function of current density, the vaporization rate of chromium from the current collector, and the magnitude of the gas diffusion coefficient. In the following subsections the reaction mechanisms and deposition of chromium in the cathode are discussed in terms of these parameters.

The goal of these simulations is to investigate the transport and reaction mechanisms of chromium in the cathode to gain a better understanding of chromium poisoning in the SOFC cathode. As discussed in Section 1, chromium is known to decrease the voltage output of the fuel cell and the effects of chromium are enhanced with current density and time. The distribution of chromium in the cathode has been seen to be concentrated in the electrochemically active region of the fuel cell near the electrolyte boundary with higher concentrations of chromium in the electrochemically active area under the current collector ribs [4]. The parametric simulations in this section are discussed in terms of these characteristics to consider the factors effecting chromium poisoning.

The simulation domain, Fig. 1, for all cases consists of a section of the cathode bounded by: the electrolyte at B_{EL}, the current collector at B_{CC} and the air channel at B_{AC}. The cathode domain is divided into two regions, the electrochemically non-active cathode, $\boldsymbol{R}_{CA}$, and the electrochemically active cathode, $\boldsymbol{R}_{EC}$. The boundary conditions for the system at the external boundaries of the cathode domain are,

$$c^{O}(\vec{x}) = C_o^{O} \quad \vec{x} \in B_{AC} \tag{34}$$

$$c^{Cr}(\vec{x}) = C_o^{Cr} \quad \vec{x} \in B_{AC} \tag{35}$$

$$\frac{\partial c^{Cr}(\vec{x})}{\partial \vec{x}} = \dot{m}_{Cr} \quad \vec{x} \in B_{CC} \tag{36}$$

$$\frac{\partial c^{o}(\vec{x})}{\partial \vec{x}} = 0 \quad \vec{x} \in B_R \cup B_L \tag{37}$$

$$\frac{\partial c^{Cr}(\vec{x})}{\partial \vec{x}} = 0 \quad \vec{x} \in B_R \cup B_L \tag{38}$$

where C_o^{O} and C_o^{Cr} are the average concentrations of oxygen and chromium at the air channel–cathode interface provided by the

Table 4
Baseline modeling conditions for the pore-scale cathode model.

Baseline conditions			References
Temperature	T	1073 K	[4]
Current density	j	0.4 A cm^{-2}	[4]
Diffusion coefficient	D	9.35E−5 m^2 s^{-1}	Calculated from Eq. (7)
Chromium mass flux	$\dot{m}_{Cr}$	3.3E−11 kg m^{-2} s^{-1}	PNNL
Oxygen mass flux	$\dot{m}_O$	3.32E−4 kg m^{-2} s^{-1}	Calculated from Eq. (33)
Oxygen adsorption rate	k_O^+	3.95E−1 m s^{-1}	[41]
Oxygen desorption rate	k_O^-	1.44E−3 kg m^{-2} s^{-1}	[41]
Chromium adsorption rate	k_{Cr}^+	3.95E−1 m s^{-1}	Assumed equal to k_O^+
Chromium desorption rate	k_{Cr}^-	1.44E−5 kg m^{-2} s^{-1}	Assumed equal to k_O^-

SOFC cell level model, Section 4, and $\dot{m}_{Cr}$ is the vaporization rate of chromium from the current collector. At all the solid boundaries within the cathode domain the competitive adsorption boundary condition, Eq. (9), is applied as discussed in Section 2, this includes the solid grains in the cathode and the solid surfaces at B_{CC} and B_{EL}. At B_{CC} the vaporization of chromium replaces the competitive adsorption reaction of chromium on that surface.

In the electrochemically active region of the cathode domain, $\boldsymbol{R}_{EC}$, a source term is added to the oxygen surface concentration equation (31) to account for the oxygen removed from the cathode due to the electrochemical reactions of the fuel cell. This is modeled as a mass flux of oxygen out of the cathode as was done in the cell level model and is calculated from the current density of the fuel cell by Eq. (33).

Initially all of the simulations contain oxygen both in the gas phase and adsorbed on the internal surfaces of the cathode, and at $t = 0$ chromium is introduced to the system through the current collector and air channel boundaries. These initial conditions correspond to typical SOFC operation, where the cathode is exposed to air before the fuel cell begins operating. Oxygen will be present in the gas of the porous cathode and will be adsorbed to the cathode surface at some level. As the fuel cell begins operation and the temperature of the fuel cell rises chromium is introduced to the cathode via vaporization from the current collector walls and begins to compete with oxygen for adsorption sites.

The baseline conditions for all of the simulations are given in Table 4. These conditions are used for each of the parametric studies presented in the following subsections.

5.2. Reaction mechanisms of chromium in the cathode

As discussed in Section 1, there are several different theories of how chromium reacts with the cathode: chemical reactions, chromium reduction reactions, chemical reactions with Mn ions. To investigate these theories we considered the effects of the chromium reaction rate and oxygen consumption on the adsorption of chromium in the cathode.

Experimental research has shown that chromium deposits primarily in $\boldsymbol{R}_{EC}$ [4]. The greatest changes in local current density in the cathode also occur in $\boldsymbol{R}_{EC}$ [54]. The local current density of the cathode is constant throughout most of the cathode and decreases in $\boldsymbol{R}_{EC}$ [54]. Based on these experimental results we believe that the chromium reaction rates should be a function of the current density, $K_{Cr} = K_{Cr}(j)$. In the pore-scale model, a step function is used to model the chromium reaction rate where the chromium reaction rate is constant throughout most of the cathode and in $\boldsymbol{R}_{EC}$ the reaction rate increases,

$$K_{Cr}^+(y) = \begin{cases} k_{Cr}^+ & y \in \boldsymbol{R}_{CA} \\ \alpha k_{Cr}^+ & y \in \boldsymbol{R}_{EC} \end{cases} \quad (39)$$

where $\alpha > 1$ and k_{Cr}^+ is assumed to be equal to k_O^+, Table 4. The desorption rate of chromium is assumed to be 100 times less than that of oxygen for all cases. Chromium adsorbs to the cathode surface and is known to react with the cathode to form spinels and Cr_2O_3, which will be strongly adsorbed to the surface; while oxygen is more likely to be weakly adsorbed to the surface.

Table 5
Chromium adsorption rates as a function of current density.

Case	Chromium adsorption rate
Kx1	$k_{Cr}^+(\boldsymbol{R}_{EC}) = 10k_{Cr}^+(\boldsymbol{R}_{CA})$
Kx2	$k_{Cr}^+(\boldsymbol{R}_{EC}) = 100k_{Cr}^+(\boldsymbol{R}_{CA})$
Kx3	$k_{Cr}^+(\boldsymbol{R}_{EC}) = 1000k_{Cr}^+(\boldsymbol{R}_{CA})$

To investigate this form of the chromium reaction rate we performed simulations with a uniform chromium reaction rate and with a variable chromium reaction rate, Eq. (39). Three different variable chromium reaction rates were considered, Table 5. Fig. 5 shows the predicted oxygen and chromium surface concentrations in the cathode from the cathode-electrolyte interface (at $y = 0\ \mu m$) through the cathode thickness to the air channel boundary ($y = 45\ \mu m$). For all three cases an increase in chromium deposition is seen in $\boldsymbol{R}_{EC}$ (Fig. 5b) with a corresponding decrease in oxygen adsorbed in $\boldsymbol{R}_{EC}$ (Fig. 5a). There is also a high deposition of chromium at the top of the cathode near the air channel boundary. Experimental imaging of the cathode has found chromium deposited near the top of the cathode in lower concentrations than in the electrochemically active area [4,55].

The magnitude of the varying chromium reaction rate affects the oxygen and chromium surface concentrations in $\boldsymbol{R}_{EC}$. The surface concentration of chromium increases and the surface concentration of oxygen decreases with increasing chromium reaction rate. The magnitude of the chromium reaction rate does not significantly affect the gas concentrations of oxygen and chromium, which are relatively constant through the cathode with a slight variation with thickness, Fig. 6.

Modeling the chromium reaction rate as a function of the current density produces deposition patterns which agree qualitatively with those seen experimentally [4]. Chromium is deposited most heavily in $\boldsymbol{R}_{EC}$ and more lightly at the top of the cathode. The results suggest that the reaction mechanisms of chromium in the cathode are related to the current density and electrons in the cathode and that electron transport should be considered in the modeling of chromium poisoning.

A uniform chromium reaction rate was also modeled and the deposition patterns are compared to the variable chromium reaction rate cases. If the reactions between chromium and the cathode are purely chemical and not related to the current density than the chromium reaction rate should be uniform throughout the cathode. The effects of the magnitude of the chromium reaction rates on the adsorption patterns of chromium in the cathode are investigated by considering five different uniform chromium adsorption reaction rates, Table 6.

The results for the five uniform chromium reaction rate cases show that as the chromium reaction rate increases, the amount of chromium adsorbed on the cathode surface increases while the amount of oxygen decreases. The distributions of chromium through the thickness of the cathode, Fig. 7b, show that at higher chromium reaction rates chromium is more heavily deposited near the air channel boundary ($y = 45\ \mu m$) and decreases through the thickness of the cathode; while oxygen displays the opposite behavior where it has the lowest concentrations at the air channel and increases through the thickness of the cathode (Fig. 7a).

These results show that chromium will displace oxygen on the LSM surface and that the deposition pattern will mirror the gas concentrations in the cathode when a uniform reaction rate is assumed, i.e. both chromium gas and surface concentrations are highest near the air channel boundary ($y = 45\ \mu m$).

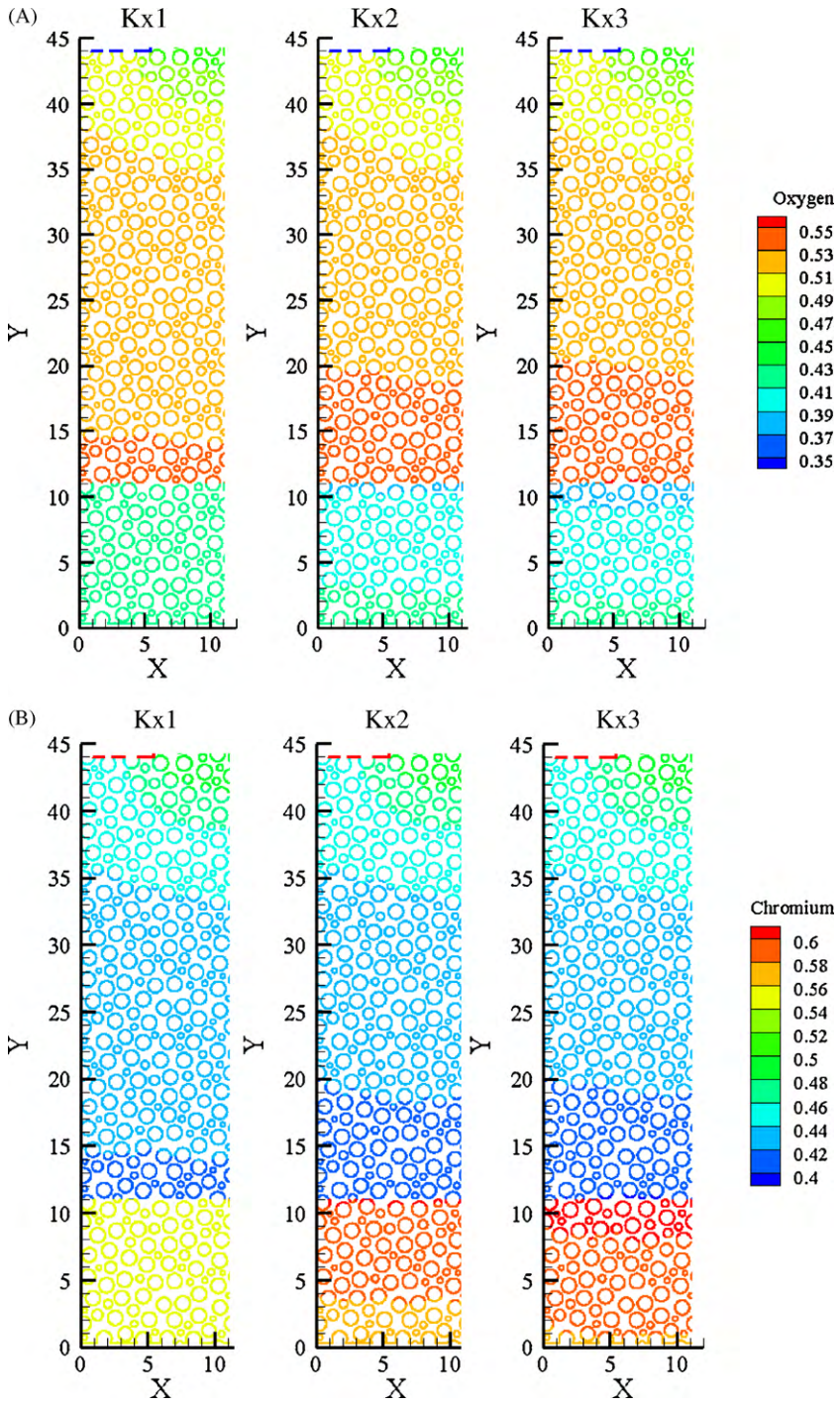

Fig. 5. Contour plots of oxygen (a) and chromium (b) surface concentrations. For each species cases Kx1 (left), Kx2 (center) and Kx3 (right) are shown. The oxygen and chromium surface concentrations are normalized by s_{max} and X and Y are in microns.

Comparing the results of the variable chromium reaction rates and the uniform chromium reaction rates show that to produce chromium depositions patterns which agree with experimental data [4] the chromium reaction rate must be a function of the local current density in the cathode. Although the results of the constant chromium reaction rate show the potential for chromium to block oxygen from adsorbing to the surface, they do not show the deposition patterns seen experimentally in chromium poisoning [4] or those seen with the variable chromium reaction rate.

It has also been theorized that chromium preferentially deposits near the electrolyte via chemical reactions (uniform reaction rates) due to the lower amounts of oxygen on the cathode surface in $\boldsymbol{R}_{EC}$ [13,56,57]. To investigate this hypothesis, we simulated three dif-

Table 6
Uniform chromium reaction rates based on the oxygen reaction rates from Table 4.

Case	Adsorption rate	Desorption rate
K1	$k_{Cr}^{+} = k_{O}^{+}/3$	$k_{Cr}^{-} = k_{O}^{-}/100$
K2	$k_{Cr}^{+} = k_{O}^{+}/1.7$	$k_{Cr}^{-} = k_{O}^{-}/100$
K3	$k_{Cr}^{+} = k_{O}^{+}$	$k_{Cr}^{-} = k_{O}^{-}/100$
K4	$k_{Cr}^{+} = 3k_{O}^{+}$	$k_{Cr}^{-} = k_{O}^{-}/100$
K5	$k_{Cr}^{+} = 30k_{O}^{+}$	$k_{Cr}^{-} = k_{O}^{-}/100$

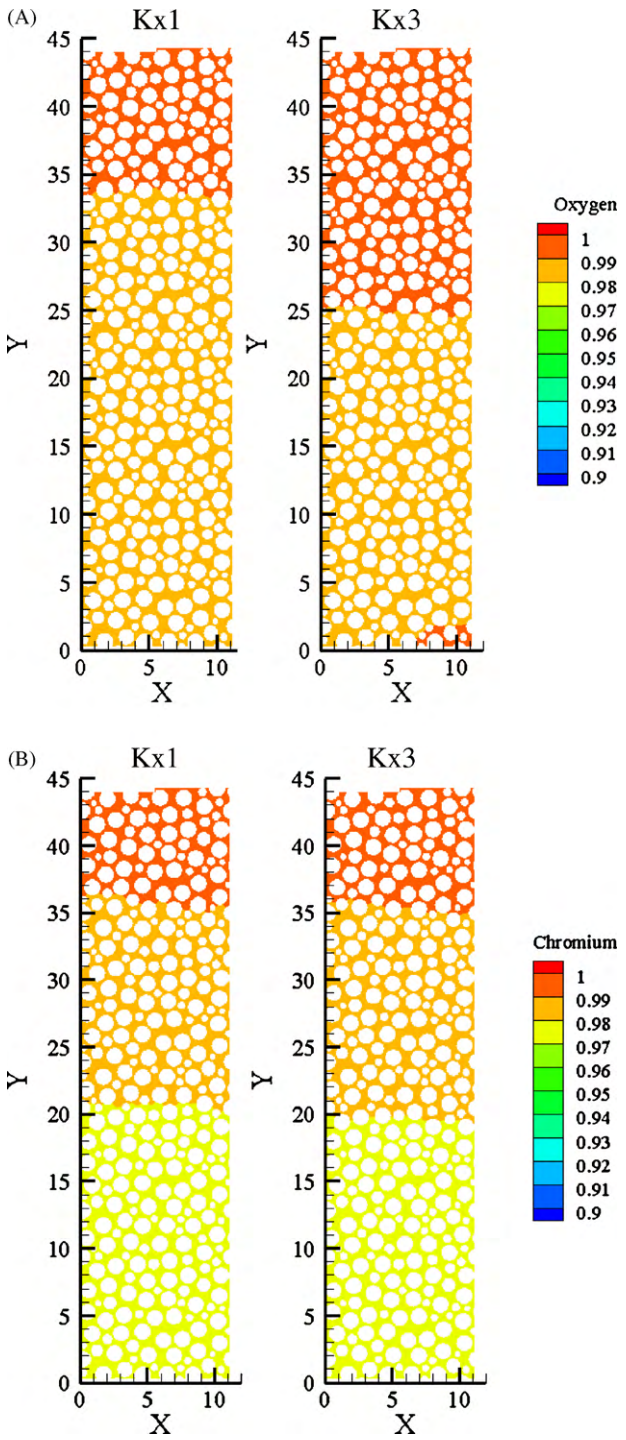

Fig. 6. Gas concentrations of oxygen (a) and chromium (b) which are shown for Kx1 (left) and Kx3 (right) for each species. The gas concentrations are normalized by the maximum concentration and X and Y are in microns.

ferent mass fluxes of oxygen out of $\boldsymbol{R}_{EC}$ with a uniform chromium reaction rate. The values of the oxygen fluxes considered are shown in Table 7 Case MO1 is calculated from the current density in Table 4 and is typical of SOFC operation; the oxygen flux of Cases MO2 and MO3 correspond to much higher current densities.

For all three cases we find that the flux of oxygen out of the cathode does not have a significant effect on the surface concentrations in the cathode. There is no noticeable decrease of oxygen in $\boldsymbol{R}_{EC}$ or increase of chromium in $\boldsymbol{R}_{EC}$, Fig. 8, where the cathode-electrolyte interface is at $y = 0$ μm. These results suggest that it is

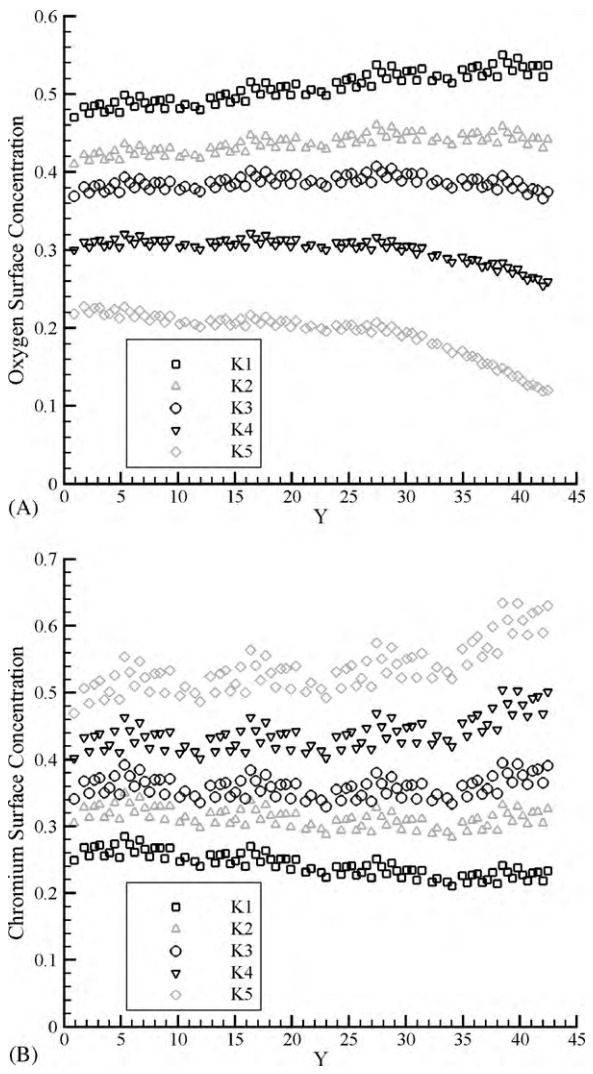

Fig. 7. Average surface concentration of oxygen (a) and chromium (b) for the five different uniform chromium reaction rates. The oxygen and chromium surface concentrations are normalized by s_{max} and Y is in microns.

not the decreased surface oxygen in $\boldsymbol{R}_{EC}$ that facilitates the preferential adsorption of chromium via chemical reactions in $\boldsymbol{R}_{EC}$ but the reaction rates and reaction mechanisms of chromium.

The results of the simulations investigating the chromium reaction mechanism and the effects of the chromium reaction rate suggest that the chromium reactions throughout the cathode are not uniform and that the driving forces for chromium reactions are related to the current density and electrochemistry of the fuel cell.

5.3. Effects of operating conditions on chromium adsorption

The operating conditions of the fuel cell can significantly affect the rate and magnitude of chromium poisoning in the SOFC cathode [4,12]. The vaporization rate and gas diffusion coefficients of chromium in the cathode were studied to consider the effects of operating temperature on chromium poisoning.

Table 7
Oxygen mass flux from the cathode surface in R_{EC}.

Case	Oxygen flux
MO1	$\dot{m}_O$
MO2	$10\dot{m}_O$
MO3	$100\dot{m}_O$

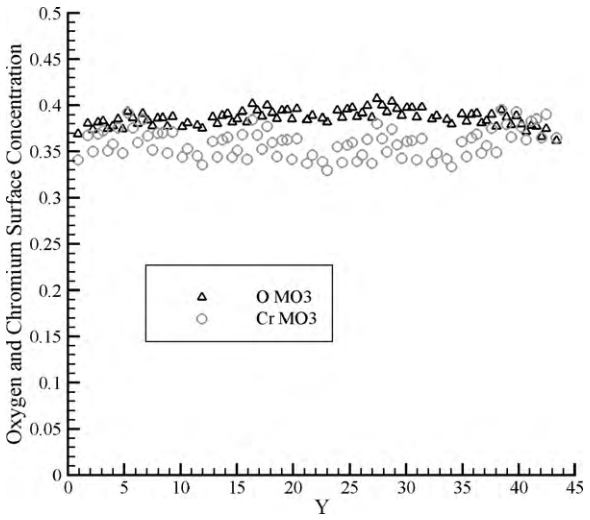

Fig. 8. Average surface concentrations through the cathode thickness for Case MO3. The oxygen and chromium surface concentrations are normalized by s_{max} and Y is in microns.

5.3.1. Vaporization rate of chromium from the current collector

Chromium is introduced to the fuel cell through the vaporization of volatile chromium species from the current collector walls. The air channel walls are composed of the current collector and, this exposes large areas of the current collector to the air flow allowing for chromium vaporization. In the porous cathode, portions of the current collector are also exposed to the air in the pore space of the cathode where the current collector interfaces with the top of the cathode, B_{CC} in our model. The rate of chromium vaporization from the current collector is a function of the humidity of the air, and the operating temperature and pressure of the fuel cell [2]. To investigate the significance of chromium vaporization at B_{CC} and to consider the effects of temperature on the vaporization rate we considered three different vaporization rates for boundary B_{CC}, Table 8.

The three chromium vaporization rates considered here are within the range of rates reported experimentally [18,52]. As the operating temperature increases the vaporization rate of chromium from the current collector increases [2]. For the three vaporization rates considered here we did not see a noticeable difference in the pattern of chromium deposition or the gas concentrations of chromium in the cathode, Fig. 9. The results suggest that chromium vaporization from the current collector at the point of contact with the cathode may not be a significant factor in chromium poisoning. The surface area of the current collector exposed to the gas at the interface with the cathode will be much smaller than the area exposed in the air channel, where most of the chromium vaporization will occur.

5.3.2. Gas diffusion rate in the cathode

The effect of the gas diffusion coefficient and the temperature (the gas diffusion coefficient is a function of the temperature, Eqs. (7) and (8)), on chromium transport in the cathode is studied by considering three different diffusion coefficients, Table 9.

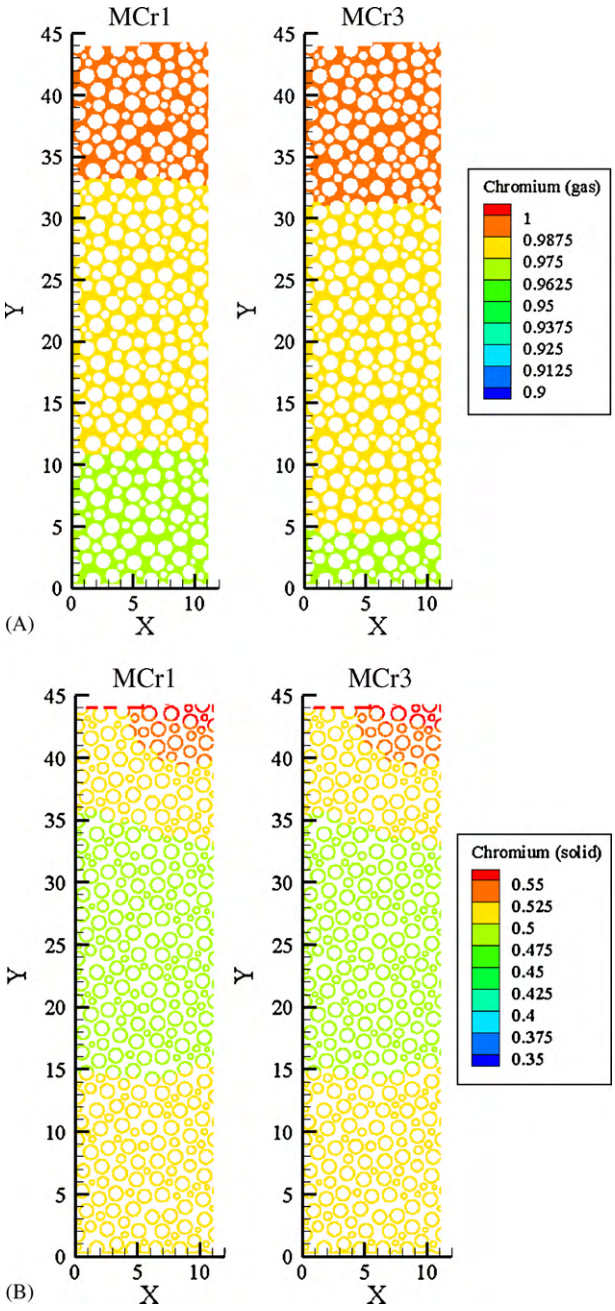

Fig. 9. Gas (a) and surface (b) concentrations of chromium for Cases MCr1 and MCr3. The gas concentrations are normalized by the maximum concentration and the surface concentrations are normalized by s_{max} and X and Y are in microns.

As seen in Fig. 10, chromium is transported through the cathode faster at higher temperatures (diffusion rates) and, as such the amount of adsorbed chromium increases with increasing temperature. The latter contradicts experimental observations that show chromium poisoning increases with decreasing temperature [3]. These results suggest that the experimentally observed

Table 8
Chromium vaporization rates from B_{CC}.

Case	Vaporization Rate
MCr1	$\dot{m}_{Cr}$
MCr2	$10\dot{m}_{Cr}$
MCr3	$100\dot{m}_{Cr}$

Table 9
Diffusion coefficients where D is the baseline diffusion coefficient, Table 4.

Case	Diffusion coefficient
D1	D
D2	$2D$
D3	$D/10$

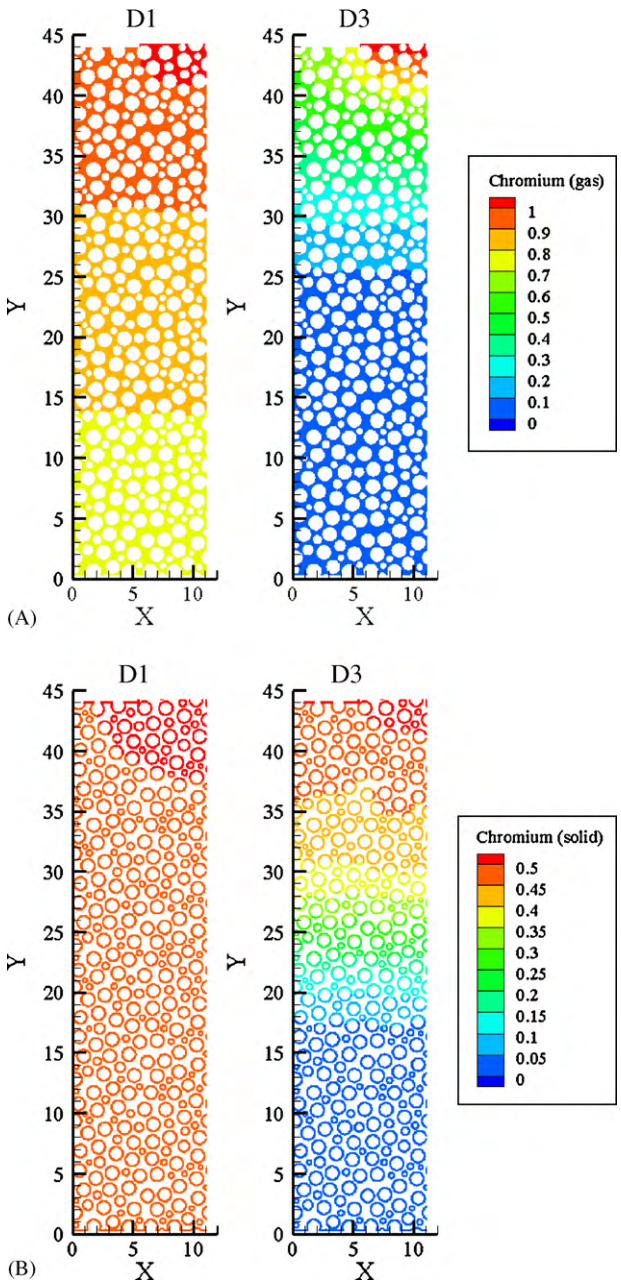

Fig. 10. Distribution of chromium in the gas (a) and on the surface (b) for cases D1 and D3. The gas concentrations are normalized by the maximum concentration and the surface concentrations are normalized by s_{max} and X and Y are in microns.

increase in chromium poisoning with decreasing temperature is due to changes in the adsorption reactions. At lower temperatures chromium may react at a much faster rate than oxygen and so be able to more efficiently block oxygen adsorption to the cathode. Well controlled experiments are needed to quantify the dependence of reaction rates on temperature.

6. Conclusions

We have presented a novel reactive transport model of chromium in an SOFC cathode. A pore-scale model was developed and used to investigate chromium poisoning. The pore-scale model is able to resolve the microstructure and physics of the SOFC cathode at a level not attainable in continuum, Darcy-scale models, of the cathode. A cell level Darcy-scale model is used to determine the boundary conditions for the pore-scale model. The pore-scale model was used to perform parametric studies of chromium poisoning including the effects of reaction rate, oxygen consumption, vaporization of chromium and diffusion rates on the distribution of chromium in the cathode, and to gain a better understanding of the transport and reaction mechanisms of chromium in the cathode.

The pore-scale model was used to interpret experimental data on the distribution of chromium in the cathode [4,55] which show an increase in chromium adsorbed in $\boldsymbol{R}_{EC}$. Parametric studies were performed to investigate the reaction mechanisms of chromium with the cathode. Simulations with uniform and spatially variable reaction rates were conducted. The simulations with uniform reaction rates produced uniform distributions of chromium throughout the cathode, which contradicts the experimental data. Increasing the consumption of oxygen in $\boldsymbol{R}_{EC}$ as suggested by [13,56,57] does not increase the chromium adsorbed in $\boldsymbol{R}_{EC}$ with a uniform chromium reaction rate.

A variable chromium reaction rate was modeled to simulate an electrochemical chromium reaction mechanism where the chromium reaction rate was modeled as a function of the current density. The variable reaction rate simulations show chromium distributions which agree qualitatively with those seen experimentally [4,55] where the highest amounts of chromium are found on the surface of the cathode in the electrochemically active area and lower amounts of chromium are found adsorbed near the top of the cathode where chromium is introduced to the cathode.

Studies of the effects of temperature on chromium poisoning were also conducted. The vaporization of chromium from the current collector increases with increasing temperature. However, simulations with increased vaporization rates from the B_{CC} boundary had no significant effects on chromium distributions in the cathode, suggesting that the small surface area of the current collector at B_{CC} is not a significant source of chromium in the system. The effects of temperature on the transport of chromium species in the cathode (diffusion coefficient) show that at lower temperatures the transport of chromium is slower than at high temperatures which should delay chromium poisoning. Experimental results have shown increased chromium poisoning at lower temperatures which suggests that the reaction rates of oxygen and chromium are a function of the temperature where chromium reacts at a faster rate than oxygen at lower temperatures.

The results of the parametric studies presented here show that the competitive adsorption of oxygen and chromium in the SOFC cathode is a complex process which is influenced by both the reaction and transport parameters of the system. The reaction rates of oxygen and chromium have the greatest effect on chromium distributions in the system and suggest that chromium poisoning is caused by electrochemically related reaction mechanisms which depend on the local current density in the cathode.

The pore-scale model resolves details of chromium poisoning that cannot be attained in coarser, cell level models and adds insight into the mechanisms of chromium poisoning. More detailed modeling of the cathode including the electrochemistry, and electron transfer could provide more realistic predictions of chromium poisoning.

Acknowledgements

The work presented in this paper was funded as part of the Solid-State Energy Conversion Alliance Core Technology Program by the U.S. Department of Energy's National Energy Technology Laboratory.

The first author was also supported by a National Science Foundation Graduate Research Fellowship.

The second author was supported by a Laboratory Directed Research and Development (LDRD) project at Pacific Northwest National Laboratory.

The Pacific Northwest National Laboratory is operated for the U.S. Department of Energy by Battelle under contract DE-AC06-76RL01830.

Appendix A. Advection in the cathode

The physical mechanisms of transport in the SOFC electrodes affect the operation, performance and degradation of SOFCs. As discussed in Section 2, gas transport in the cathode can occur due to either diffusion or advection or a combination of the two. The driving forces for advection are typically pressure gradients and/or external forces such as gravity. The design of SOFCs does not direct flow through the cathode but instead supplies air to a channel that directs flow over the top surface of the cathode creating a drag on the gas in the cathode. Under typical SOFC operating conditions, no significant pressure gradients were observed throughout the cathode [58]. A pressure gradient could arise from oxygen partial pressure changes due to the electrochemical reactions, but in SOFC operation the supply of oxygen to the cathode via the air flow is in excess of that needed for the electrochemical reactions and therefore, the partial pressure of oxygen throughout the cathode is relatively constant [54].

Here we will investigate advection in the cathode due to the flow of air over the top of the cathode. On the continuum (Darcy) scale, the drag effect of flow over the top of the cathode on the gas in the cathode can be described by the Beaver–Joseph model [59]. The flow outside a porous medium is described by the Navier–Stokes equation while the flow inside the porous medium on the continuum-scale can be described by the Darcy equation. To couple these two equations Beaver and Joseph proposed a model where the difference between the slip velocity of the free flow and the tangential component of the average pore velocity at the interface is proportional to the shear of the free flow. They were able to verify this model through experimental results and others have since theoretically proven their model [59]. The Beaver–Joseph model also allows for the calculation of the penetration depth of advection into a porous medium based on experimental parameters of the porous medium such as permeability and average pore radii [59]. Based on the typical cathode microstructural properties and the operating conditions of the SOFC [4,58], the Beaver–Joseph model predicts that the penetration depth for advection in the cathode should be ~1 μm. In a 30–50 μm thick cathode, a 1 μm advection region should not have a significant impact on the transport of species in the cathode.

To numerically investigate the significance of advection in the SOFC cathode we modeled pore-scale flow in a two-dimensional cathode ~45 μm thick with a porosity of 0.42. The pore-scale model does not necessitate any assumptions about the boundary conditions at the interface between the free flow and the porous medium, and instead solves the Navier–Stokes equation over the whole domain. The Navier–Stokes equation was solved using the SPH formulation of Tartakovsky et al. [47]. A constant velocity along the top of the simulation domain was assumed in the SPH solution. Two different flow simulations were performed with two different Reynolds numbers, 4 and 12, for the flow along the top of the porous medium. The Reynolds number is defined as,

$$Re = \frac{vL\rho}{\mu} \tag{40}$$

where L is the characteristic length of the system (air channel hydraulic diameter), v is the velocity, ρ is the density and μ is the viscosity. The higher Reynolds number case considers a velocity equal to the inlet velocity of the air channel [4], while the lower Reynolds number case uses a velocity which is 1/3 the inlet velocity.

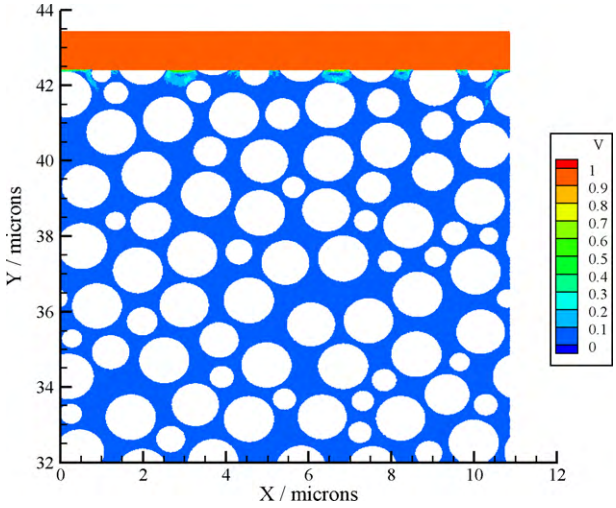

Fig. 11. Velocity contour plot for Reynolds number = 12 for the top of the cathode near the air channel. The velocity is the normalized magnitude of the velocity. *X* and *Y* are shown in microns.

As can be seen in the contour plot of Fig. 11 and the average velocity through the porous medium, Fig. 12, the velocity in the porous medium goes to zero within <1 μm from the top of the porous medium for both the high and low Reynolds number cases. The penetration depth of the pore-scale model agrees with the prediction of the Beaver–Joseph model.

The pore-scale simulation presents a simple method to determine the significance of advection in the SOFC cathode. The simple porous domain used in the pore-scale model has a higher permeability than typical SOFC cathodes [58] and uses a velocity which would be more likely to occur in the center of the air channel than at the air channel walls. These two simplifications will likely overestimate the velocity in the porous medium when compared to a real cathode geometry. A more detailed study of advection in SOFC electrodes was conducted by Resch [58] to determine its significance in SOFC modeling. Their model included the advection, diffusion, current-based reaction terms and heat transfer in an SOFC PEN assembly using a Darcy-scale model to describe the transport in

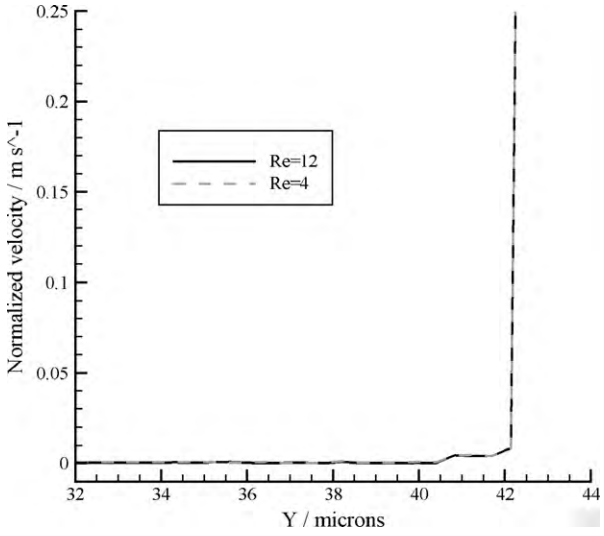

Fig. 12. Normalized average velocity through the thickness of the cathode for the top portion of the cathode near the air channel. *Y* is shown in microns. A constant velocity is applied at $Y \geq 43$.

the electrodes. Their studies agree with our pore-scale model by predicting that advection may contribute to transport in the anode but is insignificant in the cathode. Hence advection in the porous cathode is not included in the pore-scale cathode model presented in this paper.

References

[1] US Department of Energy, in: http://www1.eere.energy.gov/hydrogenandfuelcells/fuelcells/fc_types.html, Department of Energy, 2009.
[2] K. Hilpert, D. Das, M. Miller, D.H. Peck, R. Weiss, Journal of the Electrochemical Society 143 (1996) 3642–3647.
[3] M. Krumpelt, T. Cruse, B. Ingram, Proceedings of the 8th Annual SECA Workshop, DOE San Antonio, TX, 2007.
[4] T.A. Cruse, B. Ingram, D.J. Liu, M. Krumpelt, Transactions of The Electrochemical Society 5 (2007) 335–346.
[5] J.W. Fergus, International Journal of Hydrogen Energy 32 (2007) 3664–3671.
[6] E. Konysheva, H. Penkalla, E. Wessel, J. Mertens, U. Seeling, L. Singheiser, K. Hilpert, Journal of The Electrochemical Society 155 (2006) A765–A773.
[7] M.C. Tucker, H. Kurokawa, C.P. Jacobson, L.C. De Jonghe, S.J. Visco, Journal of Power Sources 160 (2006) 130–138.
[8] S.P. Jiang, J.P. Zhang, L. Apateanu, K. Foger, Journal of the Electrochemical Society 147 (2000) 4013–4022.
[9] R.A. De Souza, J.A. Kilner, Solid State Ionics 106 (1998) 175–187.
[10] R.A. De Souza, J.A. Kilner, J.F. Walker, Materials Letters 43 (2000) 43–52.
[11] J. Deseure, Y. Bultel, L. Dessemond, E. Siebert, P. Ozil, Journal of Applied Electrochemistry 37 (2007) 129–136.
[12] T.A. Cruse, M. Krumpelt, B.J. Ingram, Proceedings of the 32nd International Conference & Exposition on Advanced Ceramics and Composites, Daytona, 2008.
[13] Y. Matsuzaki, I. Yasuda, Solid State Ionics Diffusion & Reactions 132 (2000) 271–278.
[14] S. Taniguchi, M. Kadowaki, H. Kawamura, T. Yasuo, Y. Akiyama, Y. Miyake, T. Saitoh, Journal of Power Sources 55 (1995) 73–79.
[15] Y.D. Zhen, S.P. Jiang, Journal of Power Sources 180 (2008) 695–703.
[16] X. Chen, B. Hua, J. Pu, J. Li, L. Zhang, S.P. Jiang, International Journal of Hydrogen Energy 34 (2009) 5737–5748.
[17] C. Collins, J. Lucas, T.L. Buchanan, M. Kopczyk, A. Kayani, P.E. Gannon, M.C. Deibert, R.J. Smith, D.S. Choi, V.I. Gorokhovsky, Surface and Coatings Technology 201 (2006) 4467–4470.
[18] H. Kurokawa, C.P. Jacobson, L.C. DeJonghe, S.J. Visco, Solid State Ionics Diffusion & Reactions 178 (2007) 287–296.
[19] B.J. Ingram, T.A. Cruse, M. Krumpelt, Journal of the Electrochemical Society 154 (2007) 1200–1205.
[20] M. Krumpelt, T. Cruse, B. Ingram, D.J. Liu, Proceedings of the 37th Annual SECA Workshop, Philadelpia, 2006.
[21] R.S. Gemmen, J. Trembly, Journal of Power Sources 161 (2006) 1084–1095.
[22] M. Ni, D.Y.C. Leung, M.K.H. Leung, Energy Conversion and Management 50 (2009) 268–278.
[23] K. Tseronis, I.K. Kookos, C. Theodoropoulos, Chemical Engineering Science 63 (2008) 5626–5638.
[24] L. Ma, D.B. Ingham, M.C. Pourkashanian, in: I. D.B.P. Ingham (Ed.), Transport Phenomena in Porous Media III, Elsevier, Amsterdam, 2005, pp. 418–439.
[25] R. Suwanwarangkul, E. Croiset, M.W. Fowler, P.L. Douglas, E. Entchev, M.A. Douglas, Journal of Power Sources 122 (2003) 9–18.
[26] A.C. Co, V.I. Birss, Journal of Physical Chemistry B 110 (2006) 11299–11309.
[27] T. Ackmann, L.G.J. De Haart, D. Stolten, Proceedings of the Fifth European Solid Oxide Fuel Cell Forum, Lucerne, Switzerland, 2002.
[28] M. Kaviany, Principles of Heat Transfer in Porous Media, Springer, New York, 1999.
[29] Transport Phenomena in Fuel Cells, WIT Press, Boston, 2005.
[30] S.H. Chan, Z.T. Xia, Journal of the Electrochemical Society 148 (2001) 388–394.
[31] Y. Shi, N. Cai, C. Li, Journal of Power Sources 164 (2007) 639–648.
[32] W. Yuzhang, F. Yoshiba, T. Watanabe, W. Shilie, Journal of Power Sources 170 (2007) 101–110.
[33] E.L. Cussler, Diffusion: Mass Transfer in Fluid Systems, Cambridge University Press, Cambridge, 1997, pp. 104–106.
[34] L. Schmidt, The Engineering of Chemical Reactions, Oxford University Press, New York, 1998.
[35] H.-G. Hong, W. Park, Electrochemica Acta 51 (2005) 579–587.
[36] M. Ihara, T. Kusano, C. Yokoyama, Journal of The Electrochemical Society 148 (2001) A209–A219.
[37] M. Machida, Y. Kikuchi, Y. Aikawa, H. Tatsumoto, Colloids and Surfaces A: Physiochemistry 240 (2004) 179–186.
[38] T.V. Pham, P. Seshadri, P. Jackson, P. White, C.C. White, Proceedings of the 4th International Symposium on Solid Oxide Fuel Cells, Yokohama-shi, Japan, 1995, pp. 1153–1161.
[39] R.E. Williford, L.A. Chick, G.D. Maupin, S.P. Simner, J.W. Stevenson, Journal of the Electrochemical Society 150 (2003) 1067–1072.
[40] W.H. Freeman, http://acswebcontent.acs.org/games/pt.html, Chemistry in the Community, 2007.
[41] A.M. Svensson, Journal of The Electrochemical Society 144 (1997) 2719–2731.
[42] E. Ryan, A.M. Tartakovsky, C. Amon, Computer Physics Communications (submitted for publication).
[43] E. Ryan, A.M. Tartakovsky, C. Amon, Journal of Contaminant Hydrology, in press.
[44] L.B. Lucy, Astronomical Journal 82 (1977) 1013–1024.
[45] J.J. Monaghan, R.A. Gingold, Monthly Notices of the Royal Astronomical Society 181 (1977) 375–389.
[46] J.P. Morris, Y. Zhu, P.J. Fox, Computers and Geotechnics 25 (1999) 227–246.
[47] A.M. Tartakovsky, P. Meakin, T.D. Scheibe, R.M.E. West, Journal of Computational Physics 222 (2007) 654–672.
[48] A.M. Tartakovsky, P. Meakin, T.D. Scheibe, B.D. Wood, Water Resources Research 43 (2007) 05437.
[49] Y. Zhu, P.J. Fox, Transport in Porous Media 43 (2001) 441–471.
[50] J.J. Monaghan, Reports on Progress in Physics 68 (2005) 1703–1759.
[51] F. Zhao, A.V. Virkar, Journal of Power Sources 141 (2005) 79–95.
[52] M. Stanislowski, E. Wessel, K. Hilpert, T. Markus, L. Singheiser, Journal of the Electrochemical Society 154 (2007) 295–306.
[53] R. O'Hayre, S.-W. Cha, W. Colella, F. Prinz, Fuel Cell Fundamentals, John Wily and Sons, New York, 2006.
[54] W.G. Bessler, S. Gewies, M. Vogler, Electrochemica Acta 53 (2007) 1782–1800.
[55] M. Krumpelt, T.A. Cruse, M.C. Hash, 9th International Symposium on Solid Oxide Fuel Cells, SOFC IX, May 15, 2005 – May 20, 2005, Electrochemical Society Inc., Quebec, Canada, 2005, pp. 1578–1583.
[56] Y. Matsuzaki, I. Yasuda, Journal of the Electrochemical Society 148 (2001) 126–131.
[57] H. Yokokawa, T. Horita, N. Sakai, K. Yamaji, M.E. Brito, Y.P. Xiong, H. Kishimoto, Solid State Ionics Diffusion & Reactions 177 (2006) 3193–3198.
[58] E. Resch, Mechanical Engineering, Queen's University, Kingston, ON, 2008, pp. 161.
[59] W. Jager, A. Mikelic, SIAM Journal of Applied Mathematics 60 (2000) 1111–1127.